crystals

MDPI

Article

Effect of Mn^{+2} Doping and Vacancy on the Ferromagnetic Cubic 3C-SiC Structure Using First Principles Calculations

Najib M. Sultan [1], Thar M. Badri Albarody [1,*], Kingsley Onyebuchi Obodo [2] and Masri B. Baharom [1]

[1] Department of Mechanical Engineering, Universiti Teknologi PETRONAS (UTP), Bandar Seri Iskandar 32610, Perak, Malaysia
[2] HySA Infrastructure Centre of Competence, Faculty of Engineering, North-West University (NWU), Potchefstroom 2531, South Africa
* Correspondence: dher.albarody@utp.edu.my

Abstract: Wide bandgap semiconductors doped with transition metals are attracting significant attention in the fabrication of dilute magnetic semiconductor devices (DMSs). The working principle of DMSs is based on the manipulation of the electron spin, which is useful for magnetic memory devices and spintronic applications. Using the density functional theory (DFT) calculation with the GGA+U approximation, we investigated the effect of native defects on the magnetic and electronic structure of Mn+2-doped 3C-SiC structure. Three structures were selected with variations in the distance between two impurities of (Mn+2)-doped 3C-SiC, which are 4.364 Å, 5.345Å, and 6.171 Å, respectively. We found ferromagnetic coupling for single and double Mn+2 dopant atoms in the 3C-SiC structure with magnetic moments of 3 μ_B and 6 μ_B respectively. This is due to the double exchange because of p-d orbital hybridization. The p-orbitals of C atoms play important roles in the stability of the ferromagnetic configuration. The impact of Si-vacancy (nearby, far) and C-vacancy (near) of (Mn+2)-doped 3C-SiC plays an important role in the stabilization of AFM due to super-exchange coupling, while the C-vacancy (far) model is stable in FM. All electronic structures of Mn+2-doped 3C-SiC reveal a half-metallic behavior, except for the Si-vacancy and C-vacancy of (nearby), which shows a semiconductor with bandgap of 0.317 and 0.828 eV, respectively. The Curie temperature of (Mn+2)-doped 3C-SiC are all above room temperature. The study shows that native vacancies play a role in tuning the structure from (FM) to (AFM), and this finding is consistent with experiments reported in the literature.

Keywords: first principles calculation; Mn^{+2}; 3C-SiC; vacancy; electronic structure; magnetic properties

Citation: Sultan, N.M.; Albarody, T.M.B.; Obodo, K.O.; Baharom, M.B. Effect of Mn^{+2} Doping and Vacancy on the Ferromagnetic Cubic 3C-SiC Structure Using First Principles Calculations. *Crystals* **2023**, *13*, 348. https://doi.org/10.3390/cryst13020348

Academic Editors: James Ren and Paolo Restuccia

Received: 30 November 2022
Revised: 2 February 2023
Accepted: 8 February 2023
Published: 17 February 2023

1. Introduction

Dilute magnetic semiconductors (DMSs) prepared by doping with a small fraction of transition metal (TM) ions are increasingly gaining popularity for spintronics applications, as shown in Figure 1a. In the electronic industry, spintronics is important and receives significant attention [1,2]. This is because it provides a theoretical foundation, as well as technological support for the invention of the next generation of microelectronic devices [3,4]. In spintronic devices, electron charge and spin are used together to perform multiple functions [1]. The advantages of using spin-related electronic devices include, but are not limited to, an increase in the non-volatile device's data memory capacity while minimizing size and increasing data processing speed compared to conventional electronic devices. In addition, spintronic devices can be used to perform qubit (quantum bit) operations for quantum computing [2]. However, the materials traditionally used for semiconductor devices and integrated circuits, such as silicon (Si) and gallium arsenide (GaAs), do not have magnetic ions and are non-magnetic, as shown in Figure 1b, and their magnetic spins are generally rather small [2].

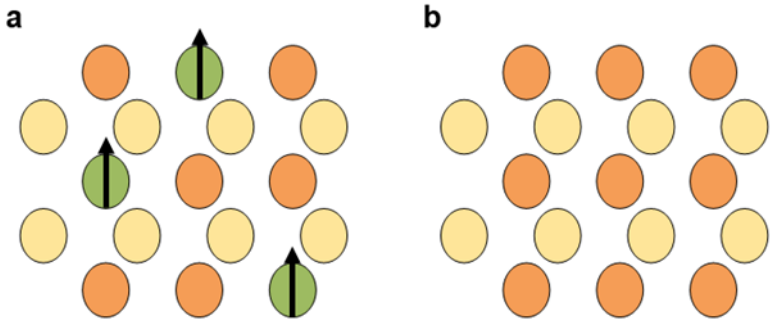

Figure 1. (**a**) Dilute magnetic semiconductor, (**b**) a nonmagnetic semiconductor, does not contain a magnetic ion.

In recent years, extensive research has been conducted on the fabrication of spintronic devices based on diluted magnetic semiconductors (DMSs) with Curie temperatures higher than room temperature [5]. Room temperature (RT) ferromagnetism has been observed in transition metal-doped semiconductors of nitride and oxide [5–7]. The *d*-orbital exchange interaction of the transition metals in DMS semiconductors is responsible for the fascinating magneto-optical and magneto-transport properties, as well as some s and *p*-orbital hybridization [8–10]. The exchange coupling hybridization of *s*, *p*, and *d*-orbitals is important in determining the nature of DMS devices [11]. The ferromagnetism observed in transition metal-doped dilute semiconductors is explained by several mechanisms, including super-exchange, Zener's double exchange, and magnetic coupling [12–15].

Notably, 3C-SiC is an intrinsic semiconductor with a cubic crystal structure that has a wide energy indirect bandgap of 2.39 eV. It has a wide range of practical applications in high voltage [16], high power [17], high thermal conductivity [18], and thermal [19] electronic devices. Due to these properties, 3C-SiC is an adequate semiconductor material for use in integrated circuits [20,21]. Silicon carbide has several phases (polytypes), with the most famous polytypes being the hexagonal, which includes 6H, 4H, and 8H, a rhombohedral polytype 15R, and a cubic polytype 3C. The 3C polytype is special as it can be synthesized at lower temperatures (1473 to 2273 K) compared to the hexagonal polytypes (2473 to 2773 K) and exhibits a high electron mobility (up to 1000 $cm^2/(Vs)$), which is attractive for the fabrication of semiconductor devices [22].

Due to the unique properties of 3C-SiC, the effect of a low transition metal (TM, where TM is Mn) dopant atom concentration is investigated. The magnetic coupling behavior and Curie temperature of the pristine and Mn^{+2} dopant configurations are evaluated as candidate materials for dilute magnetic semiconductors. The 3C-SiC can be prepared using a solid-state reaction and carbothermal reduction methods [23,24]. Ferromagnetism with a Curie temperature near room temperature was observed experimentally in Mn-doped 3C-SiC and 6H-SiC [25–27]. Additionally, Ref. [26] has reported 80 keV Mn ion implantation at room temperature ferromagnetism in the 3C-SiC (001) epilayer, and the magnetic moment per Mn increased after the implanted sample was annealed. The single crystal of 6H-SiC implanted with Mn ions was investigated and it was found that the Mn_{Si} configuration has the strongest magnetism [28]. These experiments suggest that doping Mn ions in 3C-SiC is a practical way to create DMSs. Previous study on vacancies dopants in 3C-SiC [29] were carried out; however, study on the magnetic properties is lacking. The electronic and magnetic properties of Mn-doped 6H-SiC was studied using the ab initio full potential-linearized augmented plan-wave (FPL-APW) method, and a model to explain magnetic moment was proposed [30]. Furthermore, Mn doped with 3C-SiC showed a high curie temperature and stable in ferromagnetic configuration [30,31]. The magnetic and optical properties of Mn-doped SiC nanosheets showed improved absorption in the visible region [32]. Previous studies showed that for ferromagnetism to occur and remain stable in Mn^{+2}-doped II-VI semiconductor DMSs, additional charge carriers might be introduced [33,34]. The presence of n-type carriers (or electrons) introduced by oxygen vacancies induces ferromagnetism in Mn^{+2}-doped ZnO [35]. A structure stability changes

from antiferromagnetic to ferromagnetism when a Zn vacancy is introduced to a Mn^{+2}-doped ZnTe and Te vacancy has no effect [36]. To our knowledge, several studies of Mn^{+2}-doped 3C-SiC [37–40] were carried out; however, no comprehensive studies on the presence of the vacancy of V_{Si} and V_C on Mn^{+2}-doped 3C-SiC structure were conducted, which motivated us to investigate the electronic structure stability and magnetic properties of (Mn^{+2})-doped 3C-SiC with vacancy defects as candidate systems for DMS using the first-principles calculation.

2. Computational Method

The first-principles calculations were carried out using density functional theory (DFT) [41] and projector-augmented wave (PAW) potentials [42], as implemented in the Cambridge serial total energy module (CASTEP) [43]. The study utilized Perdew Burke-Ernzerhof (PBE) of the generalized gradient approximation (GGA) to describe the exchange-correlated potential. However, it found that GGA approximation underestimates the bandgap, which has an inaccurate description of electronic and magnetic properties at the ground state of the system. In addition, GGA fails to provide a correct positioning of the d-orbitals of transition metals such as Mn, Cr, and Ni. It was discovered that hybrid functionals can correct the DFT electronic band gap underestimation, but when considering large structures, this may become computationally infeasible. To correct for the underestimation of the band gap, computationally tractable Hubbard U corrections were implemented in this study to account for the presence of electron–electron interactions [44–47]. We have selected the Hubbard U values as $U_{Si-3p} = 7.2$ eV and $U_{C-3p} = 7.2$ eV, respectively, to treat the Si-*3p* and C-*2p* valence band. In addition to that, we set the Hubbard U for Mn atom as 2.8 eV [36,48,49]. The bulk 3C-SiC crystal lattice and atomic positions were optimized using the Broyden–Fletcher–Goldfarb–Shanno (BFGS) method [50]. A cut-off plane wave energy of 420 eV was used and the ultra-soft pseudopotential was employed to treat the core electrons as valence states. To achieve good convergence, a $4 \times 4 \times 4$ Monkhorst-Pack k-point grid was selected for integration over the irreducible Brillouin zone. The space group for the 3C-SiC structure is F-43m, with a lattice constant of a = b = c = 4.348 Å, as illustrated in Figure 2a. The 3C-SiC crystal structure, depicted in Figure 2a, comprises two face-centered unit cells. The C atom is situated at the center of the tetrahedron, and the Si atom is located at the four upper corners of the tetrahedron. The primitive unit cell of 3C-SiC is shown in Figure 2b. In this work, the 3C-SiC unit cell was relaxed. The relaxed unit cell was used to build a $2 \times 2 \times 2$ supercell for the dopant and vacancy calculations. The magnetic coupling properties of the 3C-SiC supercell structure with and without different structures of Mn^{+2} doping was investigated. A Mn atom substitutionally replaced a Si atom, resulting in a Mn concentration of 3.125% to study the magnetic properties of a single (Mn^{+2})-doped 3C-SiC. Two Mn^{+2} atoms replaced Si atoms in the supercell of 3C-SiC for the magnetic coupling investigation, resulting in a Mn concentration of 6.25%. The stability of different configurations of the Mn-doped 3C-SiC compound was evaluated by calculating the formation energy of natural vacancy charge defects:

$$E_F^q = E_{defect} - E_{pure} - m\mu_{Mn} - qE_f + k\mu_{Si} \quad (1)$$

where E_{defect} and E_{pure} are the total energies of the supercell containing (Mn^{+2})-doped 3C-SiC and the perfect 3C-SiC crystal in the same supercell, respectively. m is the amount of Mn^{+2} dopant, k is the number of substituted Si atoms, respectively. μ_{Mn} and μ_{Si} are the chemical potentials of Mn and Si, respectively; q is the charge state of the defect at neutral vacancy (0). E_f is the fermi level, which is located between the top of the valance band (E_v) and the bottom of the conduction band (E_c). The chemical potentials for Si and C are not independent because both species are in thermal equilibrium with SiC, which must satisfy the thermodynamic stability condition [51]

$$\mu_{Si} + \mu_C = \mu_{SiC(bulk)} \quad (2)$$

where $\mu_{SiC(bulk)}$ is the chemical potential of SiC in the zinc-blend structure. The acceptable ranges of μ_{Si} and μ_C are established by the heat enthalpy (ΔH_f^{SiC}), which is determined as:

$$\Delta H_f^{SiC} = \mu_{SiC(bulk)} - \mu_{Si(bulk)} - \mu_{C(bulk)} \quad (3)$$

where $\mu_{SiC(bulk)}$ and $\mu_{C(bulk)}$ are the chemical potentials of Si and C, respectively, in the diamond crystal lattice, which is expressed by Equation (4) [51]

$$\Delta\mu = \mu_{Si} - \mu_{Si(bulk)} - \frac{1}{2}\Delta H_f^{SiC} = \frac{1}{2}\Delta H_f^{SiC} - \mu_C + \mu_{C(bulk)} \quad (4)$$

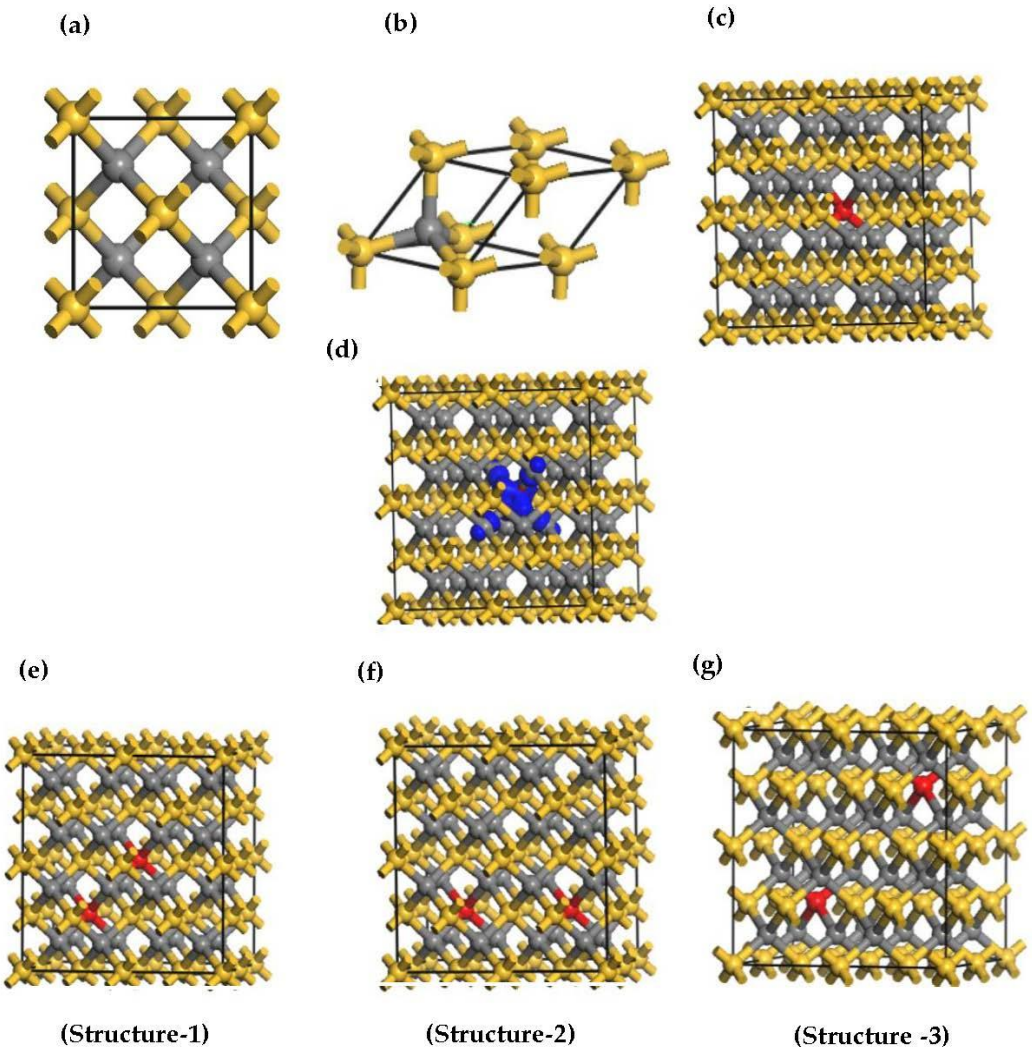

Figure 2. The optimized structures (**a**) convention unit cell of 3C-SiC, (**b**) primitive unit cell of 3C-SiC, (**c**) single (Mn^{+2})-doped 3C-SiC, (**d**) the electronic density of spin diffusion of (Mn^{+2})-doped 3C-SiC, (**e**–**g**). Three configurations of 2 atoms of (Mn^{+2})-doped 3C-SiC. Yellow, silver, and red balls indicate Si, C and Mn^{+2} respectively. The blue is iso-surface of spin distribution of the Mn^{+2} dopant.

The condition of $\mu_{Si} = \mu_{Si(bulk)}$ in a Si-rich regime and $\mu_C = \mu_{C(bulk)}$ in a C-rich regime which theoretically limits by the tuning of the C/Si ratio during growth. Thus, the lower and upper limits of the chemical potentials in Equation (3) can be defined as:

$$\frac{1}{2}\Delta H_f^{SiC} \leq \Delta\mu \leq -\frac{1}{2}\Delta H_f^{SiC} \quad (5)$$

The calculated value of the heat enthalpy ΔH_f^{SiC} was determined to be −0.62 eV/SiC, which is relatively consistent with the experimental value of −0.68 eV/SiC [52] and the theoretical work of −0.644 eV/SiC [53]. According to the result from the phonon dispersion of the 3C-SiC bulk report in [54], the structure is stable. The absence of negative vibrational modes are the main parameters determining the stability of 3C-SiC. We expect that the replacement of two Si atoms in the large supercell, which is considered in the calculation, with Mn^{+2} will not exhibit significant changes in the system stability. Our assumption agrees with the previous report of a Pd_2S_4 monolayer doped with transition metal with the presence of a vacancy defect [55] and Mn^{+2} doped with ZnTe with Zn and Te as defective vacancies [36].

3. Results and Discussion

The pristine cubic 3C-SiC unit cell was fully optimized with the calculated lattice constant of 4.169 Å, which is relatively consistent with the available experimental data of 4.359 Å [19]. The computed bandgap is 2.379 eV for the fully optimized structure, as shown in Figure 3a, which is in reasonable agreement with the experiment bandgap of 2.39 eV and the theoretical work [56]. As shown in Figure 3b, the spin up and spin down states are completely symmetrical for the total density of state (TDOS). This implies that the pristine 3C-SiC compound is a nonmagnetic structure. Figure 3c,d show the partial density of state (PDOS) of Si and C atoms respectively. The *s*- and *p*-orbitals of the Si atoms contribute to the conduction band, with *s*- and *p*-orbitals of the C atoms contributing significantly to the valance band. The conduction band and valence band exhibit a gap around the Fermi level, which confirms the semiconducting ground state.

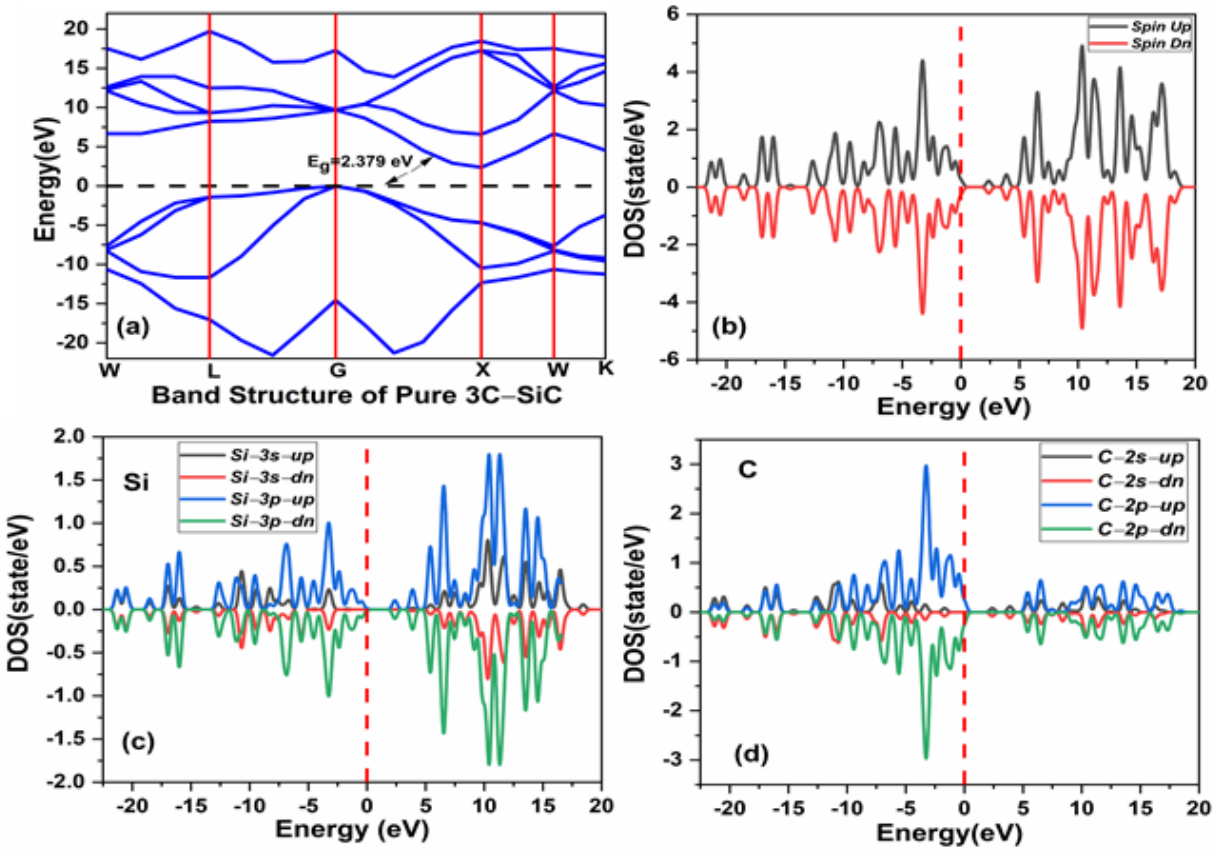

Figure 3. (**a**) The band structure of pristine 3C-SiC (**b**) spin polarized total density of states (TDOS) of pristine 3C-SiC, (**c**) partial density of state (PDOS) of Si, (**d**) and (PDOS) of C. Fermi level denoted by a black and red dash line.

To induce magnetism in the pristine 3C-SiC compound, the Mn^{+2} ion substitutes the Si atom in the $2 \times 2 \times 2$ supercell of the 3C-SiC compound, as shown in Figure 2c. This dopant concentration is equivalent to 3.125% of Mn^{+2} ion in the 3C-SiC lattice. The Hubbard U parameter for the Mn^{+2} ion (U_{Mn}) = 2.8 eV. The Hubbard U parameter provides a better description of the Mn d-orbitals. The optimized calculated bond distance of Mn-C is 1.883 Å, which is smaller than the bond length of Si-C 1.89 Å. The bond length change can be associated with the difference in the atomic radii. The atomic radius of Mn^{+2} (1.44 Å) is bigger than the atomic radius of Si (1.10 Å). The spin-polarized and non-spin-polarized total energy were calculated; we found that the spin-polarized state with a total magnetic moment of 3 μ_B is more negative compared with the non-spin-polarized state. Figure 4 shows the calculated band structure of a single Mn^{+2}-doped 3C-SiC structure. There is an exchange coupling interaction at the Fermi level due to the presence of a Mn^{+2}-ion in the 3C-SiC lattice, resulting in a half metallic character. However, the pristine 3C-SiC compound has an indirect band structure. In the spin down and spin up channel of the valence band, flat levels around −2 eV are observed, which are attributed to the Mn^{+2} dopant ion. It can be observed that the splitting of the valence band is much less than that of the conduction band. This means that the spin-splitting of the valence band is higher than the conduction band. The induced magnetism and the change in the energy band structure of the Mn^{+2}-doped 3C-SiC compound results from the *s-d* and *p-d* orbital hybridization.

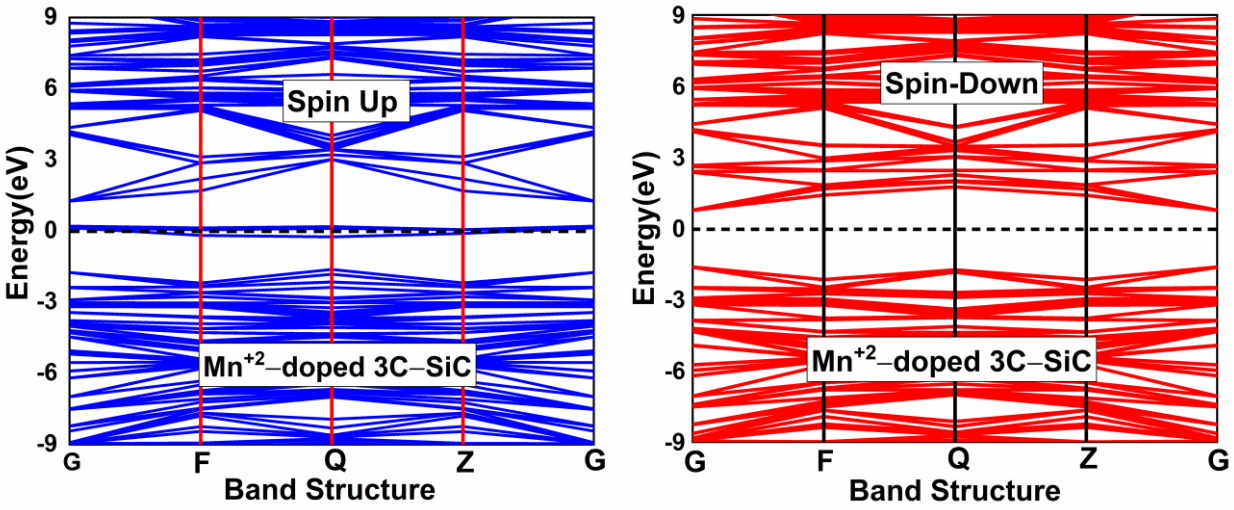

Figure 4. Spin polarized band structure of (Mn^{+2})-doped 3C-SiC. Fermi level denoted by a black dash line.

The total density of states (TDOS) and the partial density of states (PDOS) of the Mn^{+2}-doped 3C-SiC compound are calculated. An asymmetry of the up and down spin channel can be seen in the TDOS, as presented in Figure 5a. This indicates that the Mn^{+2} dopant ion results in spin changes in the lattice of the 3C-SiC. Th *p-d* hybridization is responsible for the asymmetry of the spin up and spin down states in the TDOS. At the Fermi level, the C-*2p* states and some contribution from the Si-*2p* states hybridize with the Mn-*3d* states. The C-*2p* states were observed to hybridize with the Mn- *3d* states. At the Fermi level, the strong coupling of Mn-*3d* states and 2p states of the four nearest-neighbor C atoms produce a local magnetic moment, as shown in Figure 5b. The magnetic dipole moment, mostly localized on Mn^{+2} impurities in (Mn^{+2})-doped 3C-SiC and the four nearest-neighbor of C atoms possesses a modest portion of the magnetic moment, which confirms the *p-d* hybridization, as shown in Figure 2d.

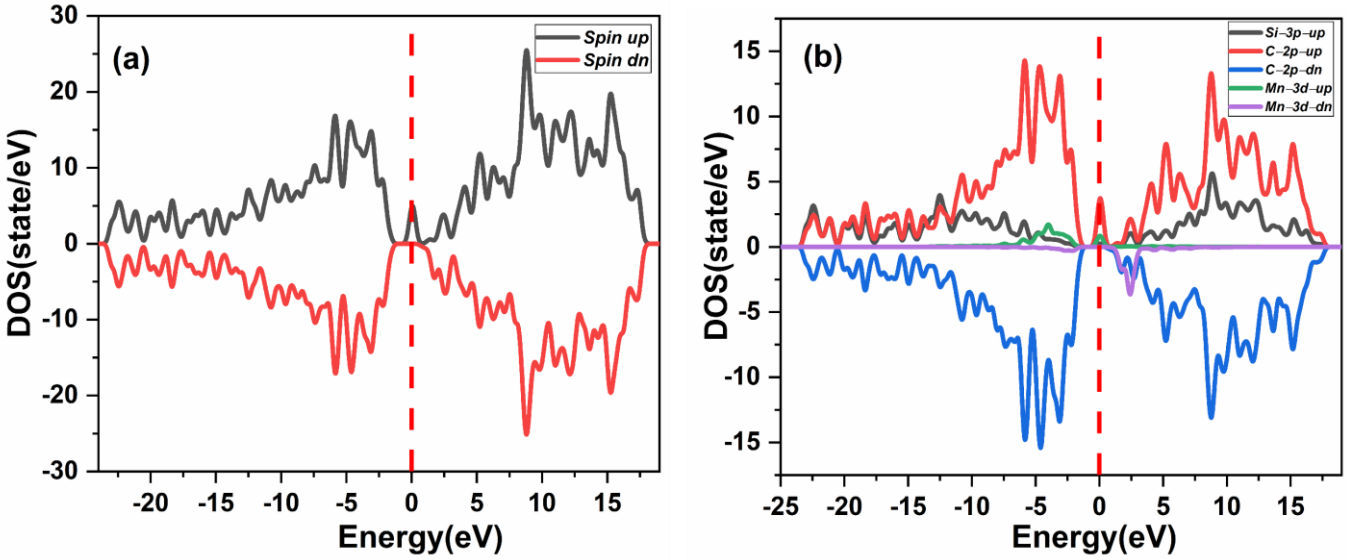

Figure 5. Spin polarized (**a**) total density of state (TDOS) and (**b**) partial DOS of (Mn^{+2})-doped 3CSiC. Fermi level denoted by a red dash line.

The orbital of (Mn^{+2})-*3d* splits into three-fold degenerate state antibonding t_{2g} ($d_{(xy)}$, $d_{(yz)}$, $d_{(xz)}$) and two-fold degenerate state nonbonding e_g ($d_{x^2-y^2}$, d_{z^2}), according to crystal tetrahedral field theory. The splitting is due to the electrostatic interaction between Mn^{+2} and four nearest neighbor C atoms [37]. The e_g ($d_{x^2-y^2}$, d_{z^2}) states are characterized by low-lying levels, while the t_{2g} ($d_{(xy)}$, $d_{(yz)}$, $d_{(xz)}$) exhibits higher-lying levels, as shown in Figure 6a. The configuration of (Mn^{+2}) is $e^2_{g\uparrow}t^3_{g\uparrow}$. As seen in Figure 5b, the majority of the Mn:*d* are not fully occupied and minority are not occupied at all at the Fermi level. The tetrahedral crystal field splitting of the antibonding state t_{2g} is weak compared to the nonbonding states of e_g as an octahedral complex system; therefore, geometric spin occupation will always be high, as illustrated in Figure 6a. All the transition metals in the first row of the periodic table exhibit weak crystal field splitting in the tetrahedral complex, including (Mn^{+2}). However, for the (Mn^{+2}) impurity doped in 3C-SiC at the silicon site, the e_g majority spin up is fully occupied and only 0.33 of the majority spin up is occupied at t_{2g} states because of the weak antibonding states of t_{2g} [32]. The accurate spin geometry orientation is $e^2_{g\uparrow}t^1_{g\uparrow}$, as shown in Figure 6b.

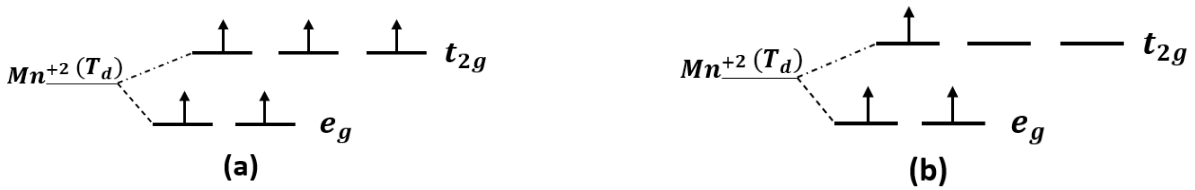

Figure 6. Geometrical spin orientation of Mn^{+2} (**a**) Mn^{+2} (T_d) at ground state, (**b**) Mn^{+2} at silicon site of doped 3C-SiC, where T_d indicated tetrahedral configuration.

3.1. Spins Coupling of Pure (Mn^{+2})-Doped 3C-SiC

To investigate magnetic coupling stability, we substituted Si atoms with two atoms of Mn^{+2} in 3C-SiC supercell, which led to a concentration of 6.25% of Mn^{+2} dopant. As illustrated in Figure 2e–g, three distinct configurations of Mn^{+2} dopant atoms were selected. The bond distance of Mn^{+2}- Mn^{+2} for configuration-1 is 4.364 Å, 5.345 Å for configuration −2 and 6.171 Å for configuration-3. The formation energy was calculated using Equation (1) and the energy difference between the FM and AFM states, with $\Delta E = E_{FM} - E_{AFM}$ determined for each structure. The result is listed in Table 1. Configuration-1 has the highest ΔE and the lowest formation energy. This means that the preferred defect structure is

configuration 1. For homogeneous Mn substitutions, it was observed that the strength of the coupling interaction diminishes as the distance between the two Mn^{+2} atoms increase. Similar results were found in ref [37].

Table 1. Calculated energy ΔE between FM and AFM for two (Mn^{+2})-doped 3C-SiC supercells, measured in meV and formation energy E_F^q in the 1, 2, and 3 structures.

Configuration	$d_{Mn1-Mn2}$ (Å)		E_F^q (meV)	$\Delta E_{FM} - \Delta E_{AFM}$ (meV)	Coupling
	Before	After			
Structure -1	4.348	4.364	2.88	−218	FM
Structure -2	5.325	5.345	3.75	−259	FM
Structure -3	6.149	6.171	4.83	−290	FM

The spin polarized TDOS and PDOS without vacancy of double (Mn^{+2})-doped 3C-SiC in the ferromagnetic configuration was investigated to ascertain the origin of its ferromagnetic character, as shown in Figure 7a,b. The two Mn dopant atoms in the 3C-SiC showed an exchange coupling state at the Fermi level. Therefore, Mn^{+2} exhibits a half metallic semiconductor as shown in Figure 7a. Furthermore, it can be shown from Figure 7b that the spin-polarized PDOS is primarily induced by the strong hybridization of the Mn-*3d* state and the C-*2p* state at the Fermi level, with the *p-d* exchange coupling, also known as Zener's double exchange coupling, being responsible for the ferromagnetism [12]. Fundamentally, the double exchange implies that *3d* or *4d* states produce coupling bands at the Fermi levels in the host band gap, resulting in partially empty bands. However, the *2p* state at the nearest-neighbor C atoms plays a major role in the stability of the ferromagnetic state. Table 1 shows that the Mn^{+2} dopant ion is stable in the FM state for the considered three structures.

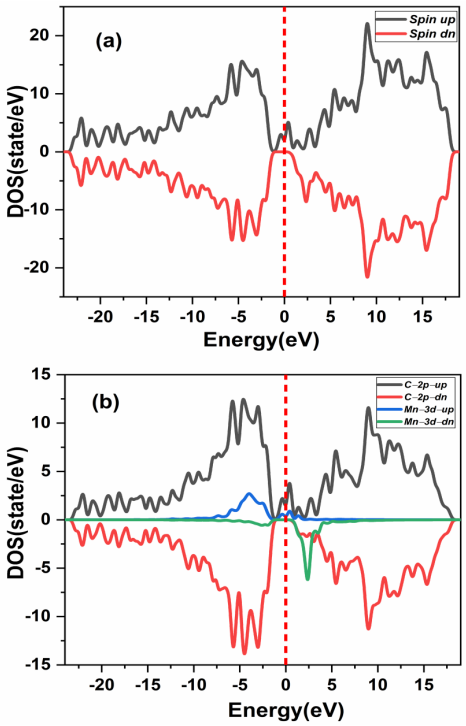

Figure 7. Spin-polarized energy of (**a**) total density of state (TDOS) and (**b**) partial DOS of double (Mn^{+2})-doped 3C-SiC. Fermi level denoted by a red dash line.

Using a simple two-level model, we can see how the magnetic state at the ground with the highest probability would be formed, as shown in Figure 8a,b. The unperturbed

exchanges split of *3d* orbitals on the isolated Mn1 and Mn2 are on the left side for FM arrangement and on the right side for AFM arrangement, respectively. In the FM arrangement, both nonbonding and antibonding levels of one spin are partially occupied, which results in energy gain due to the FM interaction. However, in the AFM arrangement, both the nonbonding and antibonding levels couple with each other, resulting in no net energy gain. Therefore, the FM coupling is energetically favorable compared to the AFM coupling.

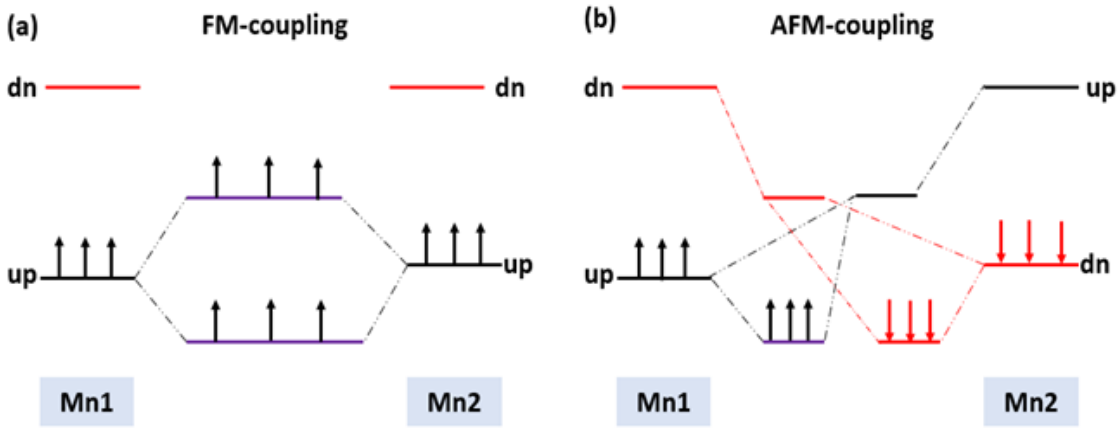

Figure 8. Schematic energy levels for two Mn interaction in the (**a**) FM and (**b**) AFM states.

3.2. Magnetic Coupling of Mn Doped 3C-SiC with Native Defect

In this section, the magnetic ground state of the Mn-doped 3C-SiC structure with native defects (i.e., vacancies) was studied, as depicted in Figure 8. The Si and C vacancies are introduced by removing one Si and C atom from the supercell. Two models for vacancy defects were selected, as illustrated in Figure 9a–d. Figure 9a is the nearby model, in which V_{si} is close to the Mn^{+2} dopant. In the far model, V_{si} is removed far from the double impurities of Mn^{+2}. The same method is also used for V_C. In the nearby model for V_C, the vacancy was inserted between (Mn^{+2})-(Mn^{+2}), as illustrated in (Figure 9c). The calculated energy difference ΔE between ferromagnetic and antiferromagnetic properties of (V_{si}, V_C) is shown in Table 2. The energy difference between FM and AFM of the Si-vacancy (nearby, far) is positive, indicating that it is stable in AFM at ground state. For V_C, the calculated energy difference of the (nearby, far) model is positive and negative, respectively. When the C-vacancy is close to the Mn^{+2} dopant atom, the resulting structure is stable in the AFM configuration. However, if the C-vacancy is far away from the (Mn^{+2})-(Mn^{+2})-doped 3C-SiC, the structure is found to be in the FM configuration. The defect due to Si-vacancy located nearby or far from the Mn^{+2}-doped 3C-SiC alters the magnetic ground state from FM to AFM. The defect due to C-vacancy, which is located near the Mn^{+2}-dopant atom in the 3C-SiC lattice, has an effect on the magnetic ground state from FM to AFM. The far defect has no effect. Both FM and AFM interaction can be induced by doping SiC with Mn ions [57], and this is related to the inhomogeneity of Mn ion distribution [24,27,57–59]. AFM ordering is observed for greater than 5% of Mn dopant atoms in 3C-SiC, thus, there is competition between the AFM and FM ordering because of the dopant [60]. The intrinsic character of the material is responsible for the magnetic ordering of the FM–AFM transition; it is not due to inhomogeneity [61–65]. We found that the Mn^{+2} ions are homogenously distributed in the 3C-SiC lattice in the presence of a native defect. This plays an important role in the magnetic transition from the FM to AFM configuration, which is consistent with the existing literature. The unperturbed exchange-split of the *3d* orbitals for isolated Mn1 and Mn2 atoms with vacancies are shown on the left and right side of Figure 10a,b for FM and AFM arrangement, respectively.

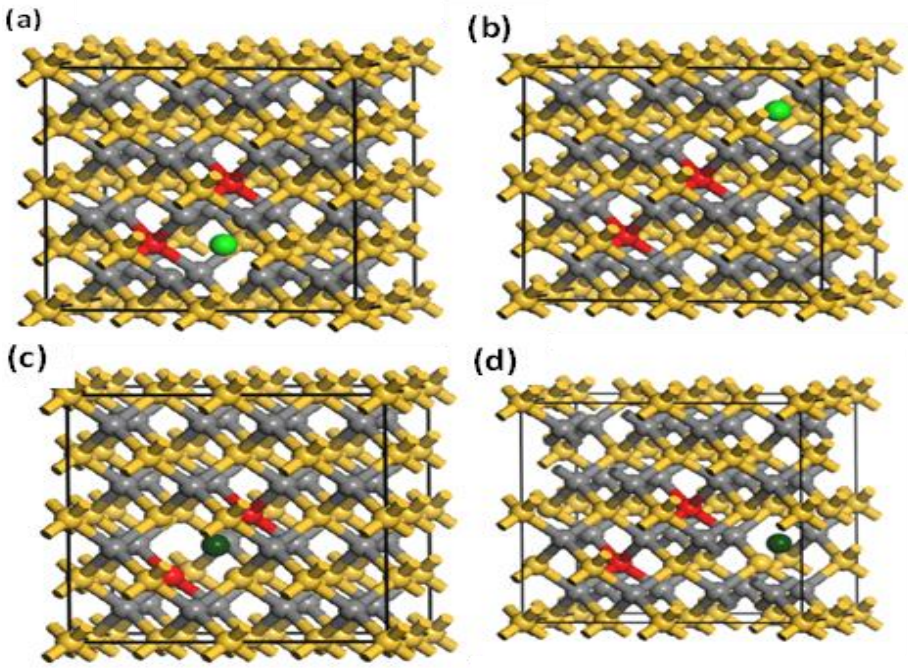

Figure 9. Nearby (**a**) and far (**b**) vacancies of $\{V_{Si}\}$-(Mn^{+2})-(Mn^{+2})-doped 3C-SiC. Models for near (**c**) and far (**d**) $\{V_C\}$-(Mn^{+2})-(Mn^{+2})-doped 3C-SiC. The red ball is for Mn^{+2}; light green and dark green indicate V_{Si} and V_C, respectively.

Table 2. Calculated energy difference $\Delta E = E_{FM} - E_{AFM}$ for two models (nearby and far) in (Mn^{+2})-doped 3C-SiC with Si and C vacancy defect. The ΔE in all models is measured by meV.

Type of Doping	ΔE (Nearby Vacancy)	ΔE (Far Vacancy)
(Mn^{+2})-doped 3C-SiC +V_{si}	398 meV	239 meV
(Mn^{+2})-doped 3C-SiC +V_c	227 meV	−405 meV

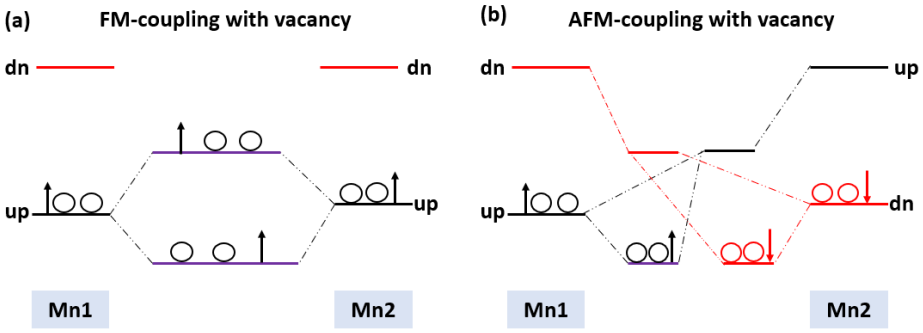

Figure 10. Schematic energy levels for two interaction Mn-*3d* with their spin (**a**) FM vacancy (**b**) AFM vacancy.

The effect of native defects in the Mn-doped SiC lattice is discussed below. The four different vacancies evaluated are as follows: (1) Si-vacancy (V_{Si}) nearby, (2) Si-vacancy (V_{Si}) far, (3) C-vacancy (V_C) nearby, (4) C-vacancy (V_C) far. These native defects in double Mn^{+2}-doped 3C-SiC lattice indicate the possibility of existence in either the AFM and FM configuration. The V_{Si} near system (see Figure 9a) has a net zero magnetic moment for the AFM ground state, having an energy difference ΔE of 398 meV compared to the FM phase (see Table 2). The band structures (see Figure 11c,d) showed that the spin down states shift slightly in higher energies compared to spin up states. There is a considerable bandgap of 0.317 eV in both spin states, implying that the V_{Si} near defect system is an antiferromagnetic

semiconductor. The total and partial DOS profile (see Figure 11a,b) showed the significant role of C-*p* and Mn-*d* orbitals in the vicinity of the Fermi energy level. Apart from the vicinity of the Fermi level, the DOS profile is symmetric when showing the AFM signature for the V_{Si} near configuration (see Figure 11a,b). Considering the V_{Si} far configuration (see Figure 9b), a similar energy shift in spin down states is observed, as depicted by the band structure (see Figure 12c,d). The DOS profile showed the symmetric distribution in both spin channels (see Figure 12a,b). This agrees with the zero magnetic moment of the configuration. For the double Mn^{+2}-doped 3C-SiC lattice with near C-vacancy (V_C near) as shown in Figure 9c, AFM is found. The spin polarized DOS are symmetrical in nature with zero magnetic moment (see Figure 13a,b). A considerable bandgap of 0.828 eV is observed in both spin states of band structure (see Figure 13c,d), which shows that the V_C near is an AFM semiconductor. Surprisingly, when a C vacancy is created at a far site (see Figure 9d) from the double Mn^{+2} cations, the V_C far defect system is metallic in nature for the spin up channel (see Figure 14c, while for the spin down channel, it is semi-conducting (see Figure 14d). Thus, the V_C far system is half metallic with a total magnetic moment of 8 μ_B. The *p-d* hybridization is observed with the spin up and the spin down state showing 100% spin polarization necessary for half metallicity (see Figure 14a,b). Furthermore, the integer value of the total magnetic moment (8 μ_B) complies well with the Slater–Pauling criteria for half metals [65]. It is pertinent to mention that all the considered vacancy configurations have intermediate states at/around the vicinity of the Fermi level due to *p-d* hybridized states. The total magnetic moments and the band structures of all studied system are summarized in Table 3.

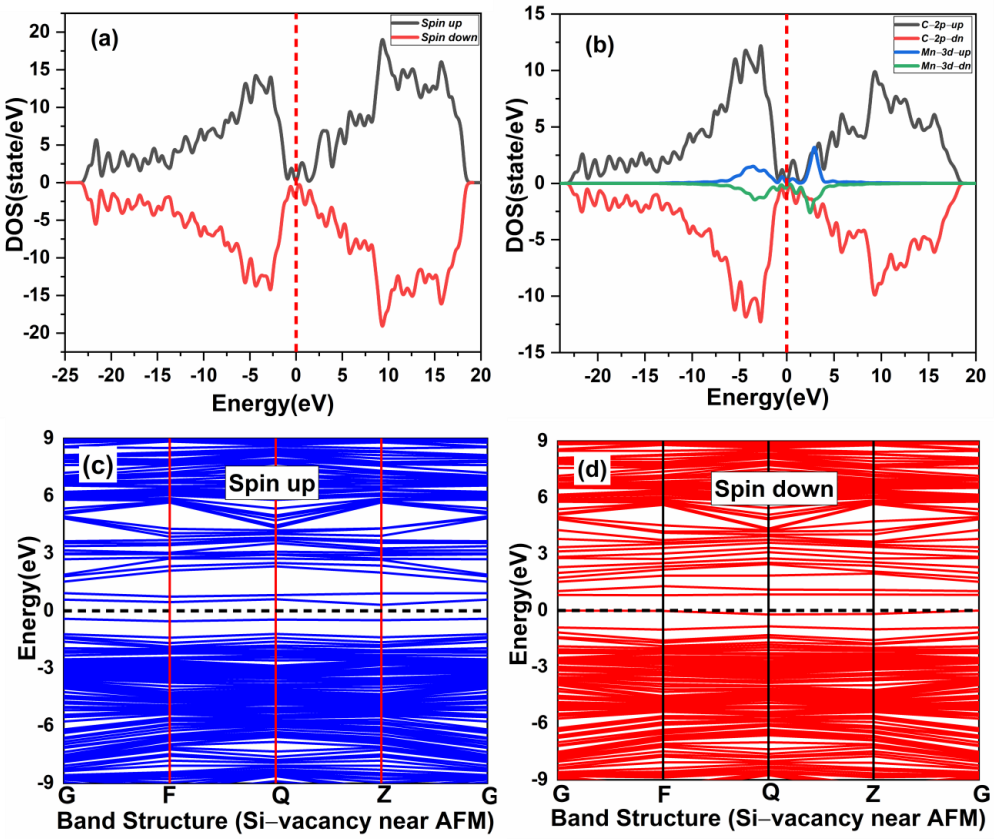

Figure 11. Spin-polarized (**a**) total density of state (TDOS) and (**b**) partial DOS of double (Mn^{+2})-doped 3C-SiC Silicon-vacancy near AFM. (**c**) Blue Spin up and (**d**) red spin down of band Structure. Fermi Level indicated by a red and black dash line.

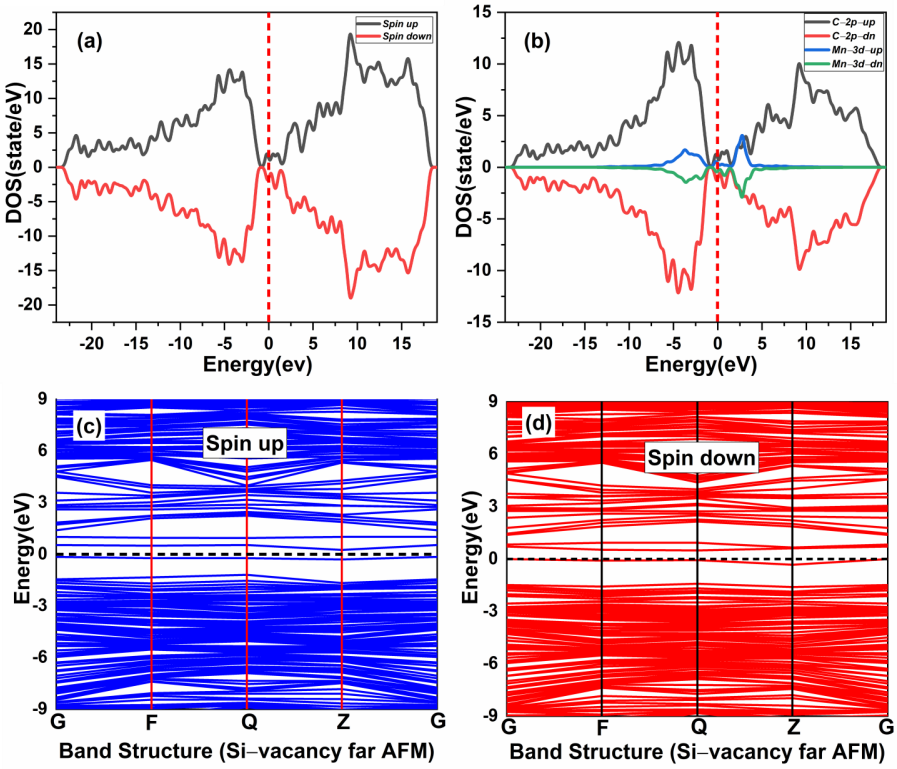

Figure 12. Spin-polarized (**a**) total density of state (TDOS) and (**b**) partial DOS of double (Mn^{+2})-doped 3C-SiC Silicon-vacancy far AFM. (**c**) Blue Spin up and (**d**) red spin down of band Structure. Fermi Level indicated by a red and black dash line.

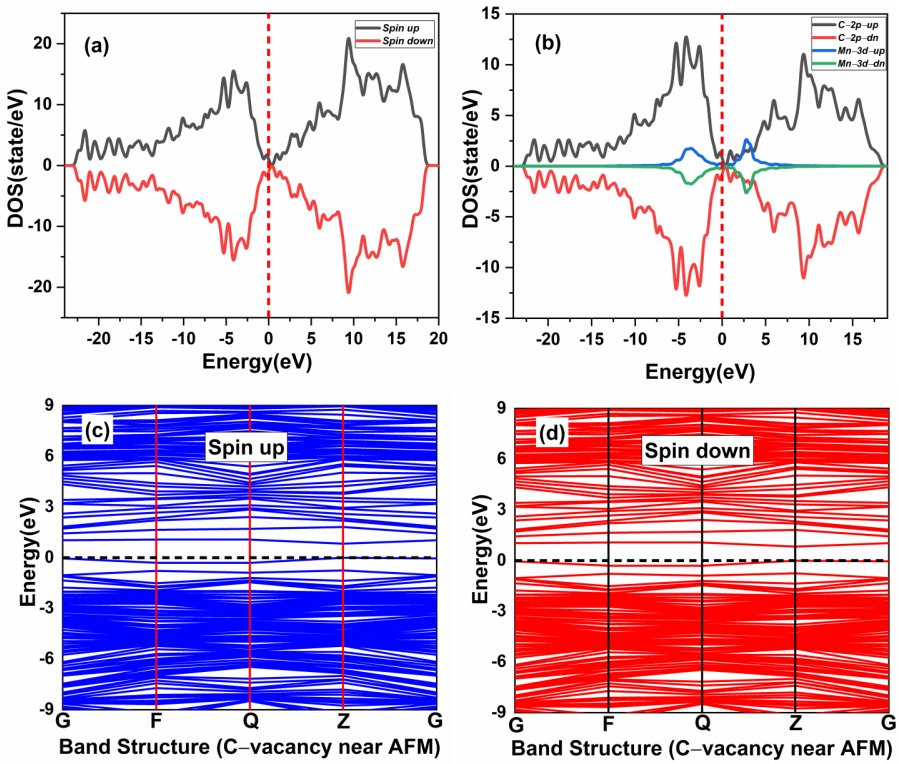

Figure 13. Spin-polarized (**a**) total density of state (TDOS) and (**b**) partial DOS. (PDOS) of double (Mn^{+2})-doped 3C-SiC Carbon-vacancy near AFM. (**c**) Blue spin up and (**d**) red spin down of band structure. Fermi Level indicated by a red and black dash line.

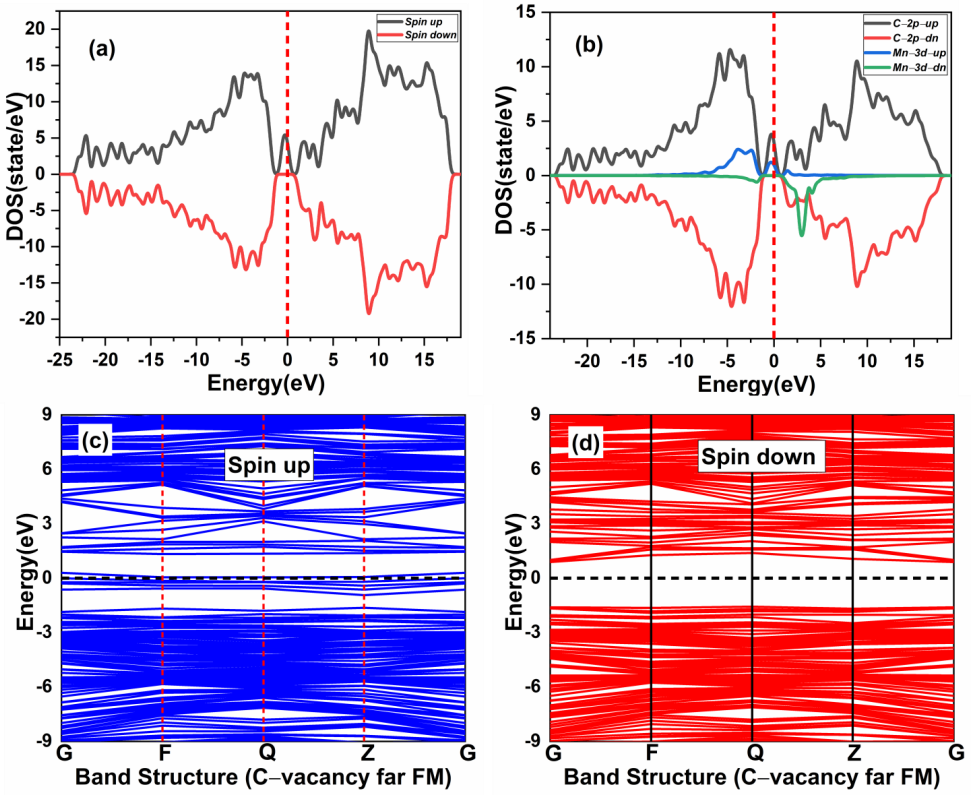

Figure 14. Spin-polarized (**a**) total density of state (TDOS) and (**b**) partial DOS (PDOS) of double (Mn^{+2})-doped 3C-SiC Carbon-vacancy far FM. (**c**) Blue spin up and (**d**) red spin down band structure. Fermi Level indicated by a red and black dash line.

Table 3. Calculated magnetic moment of (Mn^{+2})-doped 3C-SiC and band structure type of studied systems.

Type of Doping	Phase Type	Magnetic Moment (μ_B)	Band Structure Type
Pure 3C-SiC	Non-magnetic (NM)	0	2.379 eV Semiconductor
Single (Mn^{+2})-doped 3C-SiC	FM	3	Half-metallic
(Mn^{+2})-(Mn^{+2})-doped 3C-SiC	FM	6	Half metallic
(Mn^{+2})-(Mn^{+2})-doped 3C-SiC + V_{Si}(Nearby)	AFM	0	0.317 eV Semiconductor
(Mn^{+2})-(Mn^{+2})-doped 3C-SiC + V_{Si}(Far)	AFM	0	Half metallic
(Mn^{+2})-(Mn^{+2})-doped 3C-SiC + V_C(Nearby)	AFM	0	0.828 eV Semiconductor
(Mn^{+2})-(Mn^{+2})-doped 3C-SiC + V_C(Far)	FM	8	Half metallic

3.3. Curie Temperature Estimation

The Curie temperature (Tc) for single and double Mn^{+2}-doped 3C-SiC structures can be determined by taking the difference between ferromagnetic and antiferromagnetic energies, which is based on the mean-field theory and holds for diluted magnetic semiconductors. The Tc can be presented as [66,67]:

$$k_B T_C = \frac{2}{3} c \sum_{j \neq i} J_{ij} = \frac{2}{3} \Delta E / c = \frac{2}{3} \Delta E / N \quad (6)$$

where J_{ij} , c, k_B, exchange coupling constants for the two local magnetic moments at positions i and j and the concentration of Mn^{+2} and the Boltzmann constant, respectively.

T_C can be written as $T_C = \frac{2}{3}\frac{\Delta E}{Nk_B}$, where N denotes the number of the magnetic particle. According to Equation (6), the obtained Curie temperature for the Mn^{+2}-doped 3C-SiC system is shown in Table 4. The mean-field theory used to derive the Curie temperature is adequate unless for an extremely low dopant concentration [68]. The calculated Curie temperature is higher than room temperature for Mn^{+2}-doped 3C-SiC structures, irrespective of Mn^{+2} dopant atom configuration, as well as for C-vacancy (far) configuration.

Table 4. The predicated Curie temperature of (Mn^{+2})-doped 3C-SiC.

Type Configuration	Curie Temperature (k)
structure-1	843
structure-2	1000
Structure-3	1121
Nearby Si-vacancy	-
Far Si-Vacacny	-
Nearby C-vacancy	-
Far C-vacancy	1566

4. Conclusions

Density functional theory calculations were used to investigate the effect of native defects on the structural stability, electronic, and magnetic properties of a Mn^{+2}-doped 3C-SiC compound. We obtained that the ferromagnetic-induced spin polarization due to single and double Mn^{+2} dopant ions in the 3C-SiC compound is from the double exchange between the *p-d* hybridization. The *p*-orbitals of the C atoms play an important role towards the stability of the ferromagnetic character. The total magnetic moments for single and double Mn^{+2}-doped 3C-SiC are 3 μ_B and 6 μ_B respectively. The introduced Si-vacancies (near, far) have antiferromagnetic stability at the ground state of (Mn^{+2})-doped 3C-SiC. The C-vacancy (nearby) results in an AFM at ground state, while C-vacancy (far) is ferromagnetic at the ground state with a total magnetic moment of 8 μ_B. The study presents evidence that the structural stability, electronic, and magnetic properties of Mn^{+2}-doped 3C-SiC can be altered by the presence of native vacancies. This effect of native vacancies on the magnetic properties of the material was found to be consistent with prior experimental results reported in the literature. The predicted Curie temperatures are above the room temperature of the Mn^{+2}-doped 3C-SiC; as such, this configuration will be a good candidate for a spintronic device, thus, forming the basis for the synthesis of SiC-based DMSs.

Author Contributions: Conceptualization, N.M.S., T.M.B.A., K.O.O. and M.B.B.; Methodology, N.M.S., T.M.B.A., K.O.O. and M.B.B.; Software, N.M.S., T.M.B.A., K.O.O. and M.B.B.; Validation, N.M.S., T.M.B.A., K.O.O. and M.B.B.; Formal analysis, N.M.S., T.M.B.A., K.O.O. and M.B.B.; Investigation, N.M.S., T.M.B.A., K.O.O. and M.B.B.; Resources, T.M.B.A.; Data curation, N.M.S., T.M.B.A., K.O.O. and M.B.B.; Writing—original draft, N.M.S., T.M.B.A., K.O.O. and M.B.B.; Writing—review & editing, N.M.S., T.M.B.A., K.O.O. and M.B.B.; Visualization, N.M.S., T.M.B.A., K.O.O. and M.B.B.; Supervision, T.M.B.A., K.O.O. and M.B.B.; Project administration, T.M.B.A.; Funding acquisition, T.M.B.A., K.O.O. and M.B.B. All authors have read and agreed to the published version of the manuscript.

Funding: The authors would like to acknowledge Universiti Teknologi PETRONAS for its financial support under a grant (MRA-015MD0-151) and (015BD1-001), which is gratefully appreciated.

Data Availability Statement: We are continually working on this project, and the data will be used for future research and analysis. However, any researcher who needs the data for further investigations can contact the corresponding author through email with reasonable justification.

Conflicts of Interest: The authors declare no conflict of interest.

References

1. Wolf, S.A.; Awschalom, D.D.; Buhrman, R.A.; Daughton, J.M.; von Molnár, S.; Roukes, M.L.; Chtchelkanova, A.Y.; Treger, D.M. Spintronics: A Spin-Based Electronics Vision for the Future. *Science* **2001**, *294*, 1488–1495. [CrossRef] [PubMed]
2. Ohno, H. Making Nonmagnetic Semiconductors Ferromagnetic. *Science* **1998**, *281*, 951–956. [CrossRef] [PubMed]
3. Dietl, T.; Ohno, H.; Matsukura, F.; Cibert, J.; Ferrand, D. Zener Model Description of Ferromagnetism in Zinc-Blende Magnetic Semiconductors. *Science* **2000**, *287*, 1019–1022. [CrossRef] [PubMed]
4. Jungwirth, T.; Sinova, J.; Mašek, J.; Kučera, J.; MacDonald, A.H. Theory of ferromagnetic (III,Mn)V semiconductors. *Rev. Mod. Phys.* **2006**, *78*, 809–864. [CrossRef]
5. Griffin, K.A.; Pakhomov, A.B.; Wang, C.M.; Heald, S.M.; Krishnan, K.M. Intrinsic Ferromagnetism in Insulating Cobalt Doped Anatase TiO_2. *Phys. Rev. Lett.* **2005**, *94*, 157204. [CrossRef]
6. Hong, N.H.; Sakai, J.; Prellier, W.; Hassini, A.; Ruyter, A.; Gervais, F. Ferromagnetism in transition-metal-doped TiO_2 thin films. *Phys. Rev. B* **2004**, *70*, 195204. [CrossRef]
7. Liu, X.; Lin, F.; Sun, L.; Cheng, W.; Ma, X.; Shi, W. Doping concentration dependence of room-temperature ferromagnetism for Ni-doped ZnO thin films prepared by pulsed-laser deposition. *Appl. Phys. Lett.* **2006**, *88*, 062508. [CrossRef]
8. Javid, H.; Aldaghfag, S.A.; Butt, M.K.; Mubashir, S.; Yaseen, M.; Ishfaq, M.; Saleem, S.; Ali, H.E.; Hegazy, H.H. Physical characteristics of $LaCr_xAl_{1-x}O_3$: DFT approach. *J. Ovonic Res.* **2022**, *18*, 481–489. [CrossRef]
9. Arshad, M.; Yaseen, M.; Aldaghfag, S.A.; Saleem, S.; Ishfaq, M.; Nazar, M.; Yousef, E.; Hegazy, H.H. Physical characteristics of $Pb_{1-x}A_xSe$ (A = Fe, Mn, V) for spintronic applications. *Chalcogenide Lett.* **2022**, *19*, 553–563. [CrossRef]
10. Katayama-Yoshida, H.; Sato, K. Spin and charge control method of ternary II–VI and III–V magnetic semiconductors for spintronics: Theory vs. experiment. *J. Phys. Chem. Solids* **2003**, *64*, 1447–1452. [CrossRef]
11. Saito, H.; Zayets, V.; Yamagata, S.; Ando, K. Room-Temperature Ferromagnetism in a II–VI Diluted Magnetic Semiconductor $Zn_{1-x}Cr_xTe$. *Phys. Rev. Lett.* **2003**, *90*, 207202. [CrossRef] [PubMed]
12. Anderson, P.W. Antiferromagnetism. Theory of Superexchange Interaction. *Phys. Rev.* **1950**, *79*, 350. [CrossRef]
13. Ysl, P.; Ew, C.R.E. Interaction Between the d SheHs in the Transition Metals. *Phys. Rev.* **1951**, *81*, 440.
14. Tian, Z.; Yuan, S.; He, J.; Li, P.; Zhang, S.; Wang, C.; Wang, Y.; Yin, S.; Liu, L. Structure and magnetic properties in Mn doped SnO2 nanoparticles synthesized by chemical co-precipitation method. *J. Alloy. Compd.* **2008**, *466*, 26–30. [CrossRef]
15. Kaminski, A.; Das Sarma, S. Polaron Percolation in Diluted Magnetic Semiconductors. *Phys. Rev. Lett.* **2002**, *88*, 247202. [CrossRef]
16. Xun, Q.; Xun, B.; Li, Z.; Wang, P.; Cai, Z. Application of SiC power electronic devices in secondary power source for aircraft. *Renew. Sustain. Energy Rev.* **2017**, *70*, 1336–1342. [CrossRef]
17. Wang, Z.; Shi, X.; Tolbert, L.M.; Wang, F.; Liang, Z.; Costinett, D.; Blalock, B.J. A high temperature silicon carbide mosfet power module with integrated silicon-on-insulator-based gate drive. *IEEE Trans. Power Electron.* **2014**, *30*, 1432–1445. [CrossRef]
18. Goela, J.S.; Brese, N.E.; Burns, L.E.; Pickering, M.A. High-Thermal-Conductivity SiC and Applications. In *High Thermal Conductivity Materials*; Springer-Verlag: Berlin, Germany, 2006; pp. 167–198. [CrossRef]
19. Sultan, N.M.; Albarody, T.M.B.; Al-Jothery, H.K.M.; Abdullah, M.A.; Mohammed, H.G.; Obodo, K.O. Thermal Expansion of 3C-SiC Obtained from In-Situ X-ray Diffraction at High Temperature and First-Principal Calculations. *Materials* **2022**, *15*, 6229. [CrossRef]
20. Amy, F.; Douillard, L.; Aristov, V.Y.; Soukiassian, P. Oxynitridation of cubic silicon carbide (100) surfaces. *J. Vac. Sci. Technol. A* **1999**, *17*, 2629–2633. [CrossRef]
21. Fraga, M.A.; Bosi, M.; Negri, M. Silicon Carbide in Microsystem Technology—Thin Film Versus Bulk Material. In *Advanced Silicon Carbide Devices and Processing*; Saddow, S.E., Via, F.L., Eds.; InTech: London, UK, 2015. [CrossRef]
22. Gorin, S.N.; Ivanova, L.M. Cubic Silicon Carbide (3C-SiC): Structure and Properties of Single Crystals Grown by Thermal Decomposition of Methyl Trichlorosilane in Hydrogen. *Phys. Status Solidi B* **1997**, *202*, 221–245. [CrossRef]
23. Zheng, H.W.; Wang, Z.Q.; Liu, X.Y.; Diao, C.L.; Zhang, H.R.; Gu, Y.Z. Local structure and magnetic properties of Mn-doped 3C-SiC nanoparticles. *Appl. Phys. Lett.* **2011**, *99*, 222512. [CrossRef]
24. Ma, S.; Sun, Y.; Zhao, B.; Tong, P.; Zhu, X.; Song, W. Magnetic properties of Mn-doped cubic silicon carbide. *Phys. B Condens. Matter* **2007**, *394*, 122–126. [CrossRef]
25. Sun, X.; Guo, R.; An, Y.; Liu, J. Investigation of structure, magnetic, and transport properties of Mn-doped SiC films. *J. Vac. Sci. Technol. A* **2013**, *31*, 41507. [CrossRef]
26. Bouziane, K.; Al Azri, M.; Elzain, M.; Chérif, S.; Mamor, M.; Declémy, A.; Thomé, L. Mn fraction substitutional site and defects induced magnetism in Mn-implanted 6H-SiC. *J. Alloy. Compd.* **2015**, *632*, 760–765. [CrossRef]
27. Al Azri, M.; Elzain, M.; Bouziane, K.; Chérif, S.M.; Roussigné, Y.; Declemy, A.; Drouet, M.; Thomé, L. Magnetic properties of Mn-implanted 6H-SiC single crystal. *J. Appl. Phys.* **2012**, *111*, 07C315. [CrossRef]
28. Lu, X.; Yang, P.; Luo, J.; Guo, X.; Ren, J.; La, P. Density functional theory capture of electronic structures and optical properties of vacancy doped 3C-SiC systems. *Mater. Res. Express* **2019**, *6*, 115905. [CrossRef]
29. Al Azri, M.; Elzain, M.; Bouziane, K.; Chérif, S.M. First principal calculation of the electronic and magnetic properties of Mn-doped 6H-SiC. *Eur. Phys. J. B* **2013**, *86*, 402. [CrossRef]
30. Takano, F.; Wang, W.; Ofuchi, H.; Ohshima, T.; Akinaga, H.; Caldas, M.; Studart, N. Structural and Magnetic Properties of Mn-Doped SiC. *AIP Conf. Proc.* **2010**, *1199*, 443. [CrossRef]

31. Tang, S.-A.; Mao, F.; Zhao, X.-D.; Zhang, C. First-principles study of the ferromagnetism of Mn-doped 3C-SiC. *Solid State Commun.* **2020**, *321*, 114039. [CrossRef]
32. Houmad, M.; Dakir, O.; Benzidi, H.; Mounkachi, O.; El Kenz, A.; Benyoussef, A. Magnetic behavior of Mn-doped silicon carbide nanosheet. *Int. J. Mod. Phys. B* **2017**, *31*, 1750163. [CrossRef]
33. Sato, K.; Katayama-Yoshida, H. Ab initio Study on the Magnetism in ZnO-, ZnS-, ZnSe-and ZnTe-Based Diluted Magnetic Semiconductors. *Phys. Stat. Sol.* **2002**, *229*, 673–680. [CrossRef]
34. Iuşan, D.; Sanyal, B.; Eriksson, O. Role of defects on the magnetic interactions in Mn-doped ZnO. *Phys. Status Solidi A* **2007**, *204*, 53–60. [CrossRef]
35. Kittilstved, K.; Liu, W.K.; Gamelin, D.R. Electronic structure origins of polarity-dependent high-TC ferromagnetism in oxide-diluted magnetic semiconductors. *Nat. Mater.* **2006**, *5*, 291–297. [CrossRef] [PubMed]
36. Khan, M.S.; Shi, L.-J.; Abdalla, A.; Zou, B.; Ikram, M. Computational insights into electronic, magnetic and optical properties of Mn(II)-doped ZnTe with and without vacancy defects. *Mater. Sci. Semicond. Process.* **2022**, *150*, 106965. [CrossRef]
37. Lin, X.-L.; Zhang, H.-X.; Yang, W.-X.; Chen, H.-M.; Pan, F.-C. The high Curie temperature and long-range ferromagnetism in Mn-doped 3C-SiC: A study using first-principles calculation. *J. Korean Phys. Soc.* **2021**, *79*, 546–551. [CrossRef]
38. Moharana, G.P.; Singh, S.K.; Narayanan, H.K. Ferromagnetism in Mn doped 3C-SiC: A variable temperature ESR study. *J. Magn Magn Mater.* **2021**, *527*, 167707. [CrossRef]
39. Izadifard, M.; Ghazi, M.E.; Hosaini, S. Effects of Mn Substitution on Magnetic and Electronic Properties of β-SiC Semiconductor. *Appl. Phys. Res.* **2010**, *2*, 2. [CrossRef]
40. Patnaik, P.; Mukhopadhyay, G.; Singh, P.P.; Garg, A.B.; Mittal, R.; Mukhopadhyay, R. Magnetism in Transition metal doped Cubic SiC. *AIP Conf. Proc.* **2011**, *1349*, 1087. [CrossRef]
41. Kohn, W.; Sham, L.J. Self-consistent equations including exchange and correlation effects. *Phys. Rev.* **1965**, *140*, A1133. [CrossRef]
42. Blochl, P.E. Projector augmented-wave method. *Phys. Rev. B* **1994**, *50*, 17953. [CrossRef]
43. Segall, M.D.; Lindan, P.J.D.; Probert, M.J.; Pickard, C.J.; Hasnip, P.J.; Clark, S.J.; Payne, M.C. First-principles simulation: Ideas, illustrations and the CASTEP code. *J. Phys. Condens. Matter* **2002**, *14*, 2717–2744. [CrossRef]
44. Ouma, C.N.M.; Singh, S.; Obodo, K.O.; Amolo, G.O.; Romero, A.H. Controlling the magnetic and optical responses of a MoS_2 monolayer by lanthanide substitutional doping: A first-principles study. *Phys. Chem. Chem. Phys.* **2017**, *19*, 25555–25563. [CrossRef]
45. Mulwa, W.M.; Ouma, C.N.; Onani, M.O.; Dejene, F.B. Energetic, electronic and optical properties of lanthanide doped TiO2: An ab initio LDA+U study. *J. Solid State Chem.* **2016**, *237*, 129–137. [CrossRef]
46. Obodo, K.; Chetty, N. First principles LDA +*U*and GGA +*U*study of protactinium and protactinium oxides: Dependence on the effective*U*parameter. *J. Phys. Condens. Matter* **2013**, *25*, 145603. [CrossRef]
47. Obodo, K.; Chetty, N. GGA+U studies of the early actinide mononitrides and dinitrides. *J. Nucl. Mater.* **2013**, *442*, 235–244. [CrossRef]
48. Lin, L.; Yao, L.; Li, S.; Shi, Z.; Xie, K.; Huang, J.; Tao, H.; Zhang, Z. Influence of Mn and Co doping on optical and magnetic properties in 3C–SiC. *J. Phys. Chem. Solids* **2021**, *153*, 110002. [CrossRef]
49. Cockayne, E.; Levin, I.; Wu, H.; Llobet, A. Magnetic structure of bixbyite α-Mn_2O_3: A combined DFT+U and neutron diffraction study. *Phys. Rev. B* **2013**, *87*, 184413. [CrossRef]
50. Fletcher, R. *Practical Methods of Optimization*; Wiley: New York, NY, USA, 1981; Volume 1.
51. Aradi, B.; Gali, A.; Deák, P.; Lowther, J.E.; Son, N.T.; Janzén, E.; Choyke, W.J. *Ab initio* density-functional supercell calculations of hydrogen defects in cubic SiC. *Phys. Rev. B* **2001**, *63*, 245202. [CrossRef]
52. Madelung, O.; Schulz, M.; Weiss, H. *Numerical Data and Functional Relationships in Science and Technology*, 2 nd ed; Springer: New York, NY, USA, 1982.
53. Dou, Y.; Jin, H.-B.; Cao, M.; Fang, X.; Hou, Z.; Li, D.; Agathopoulos, S. Structural stability, electronic and optical properties of Ni-doped 3C–SiC by first principles calculation. *J. Alloy. Compd.* **2011**, *509*, 6117–6122. [CrossRef]
54. Zhao, Q.; Zhang, Z.; Li, Y.; Ouyang, X. The mechanical and thermodynamic properties of β-$Si_{1-x}C$. *RSC Adv.* **2017**, *7*, 28499–28505. [CrossRef]
55. Gholami, M.; Golsanamlou, Z.; Soleimani, H.R. Effects of 3D transition metal impurities and vacancy defects on electronic and magnetic properties of pentagonal Pd_2S_4: Competition between exchange splitting and crystal fields. *Sci. Rep.* **2022**, *12*, 10838. [CrossRef] [PubMed]
56. Schultz, P.A.; Van Ginhoven, R.M.; Edwards, A.H. Theoretical study of intrinsic defects in cubic silicon carbide 3C-SiC. *Phys. Rev. B* **2021**, *103*, 195202. [CrossRef]
57. Yang, J.; Song, W.H.; Ma, Y.Q.; Zhang, R.L.; Zhao, B.C.; Sheng, Z.G.; Zheng, G.H.; Dai, J.M.; Sun, Y.P. Structural, magnetic, and transport properties in thePr-doped manganites $La_{0.9-x}Pr_xTe_{0.1}MnO_3$ ($0 \leq x \leq 0.9$). *Phys. Rev. B* **2004**, *70*, 144421. [CrossRef]
58. Song, B.; Bao, H.; Li, H.; Lei, M.; Jian, J.; Han, J.; Zhang, X.; Meng, S.; Wang, W.; Chen, X. Magnetic properties of Mn-doped 6H-SiC. *Appl. Phys. Lett.* **2009**, *94*, 102508. [CrossRef]
59. Bolduc, M.; Awo-Affouda, C.; Stollenwerk, A.; Huang, M.B.; Ramos, F.G.; Agnello, G.; LaBella, V.P. Above room temperature ferromagnetism in Mn-ion implanted Si. *Phys. Rev. B* **2005**, *71*, 033302. [CrossRef]
60. Moharana, G.P.; Singh, S.; Babu, P.; Narayanan, H.K. Investigation of magnetic order and spin dynamics in Mn doped 3C-SiC. *J. Alloy. Compd.* **2018**, *765*, 314–323. [CrossRef]

61. Chattopadhyay, M.K.; Roy, S.B.; Chaddah, P. Kinetic arrest of the first-order ferromagnetic-to-antiferromagnetic transition in $Ce(Fe_{0.96}Ru_{0.04})_2$: Formation of a magnetic glass. *Phys. Rev. B* **2005**, *72*, 180401. [CrossRef]
62. Sokhey, K.; Chattopadhyay, M.; Nigam, A.; Roy, S.; Chaddah, P. Signatures of phase separation across the disorder broadened first order ferromagnetic to antiferromagnetic transition in doped-$CeFe_2$ alloys. *Solid State Commun.* **2004**, *129*, 19–23. [CrossRef]
63. Roy, S.B.; Perkins, G.K.; Chattopadhyay, M.K.; Nigam, A.K.; Sokhey, K.J.S.; Chaddah, P.; Caplin, A.D.; Cohen, L.F. First Order Magnetic Transition in Doped $CeFe_2$ Alloys: Phase Coexistence and Metastability. *Phys. Rev. Lett.* **2004**, *92*, 147203. [CrossRef]
64. Chattopadhyay, M.K.; Roy, S.B.; Nigam, A.K.; Sokhey, K.J.S.; Chaddah, P. Metastability and giant relaxation across the ferromagnetic to antiferromagnetic transition in $Ce(Fe_{0.96}Ru_{0.04})_2$. *Phys. Rev. B* **2003**, *68*, 174404. [CrossRef]
65. Galanakis, I. Slater-Pauling Behavior in Half-Metallic Magnets. *J. Surfaces Interfaces Mater.* **2014**, *2*, 74–78. [CrossRef]
66. Tan, Z.; Xiao, W.; Wang, L.; Yang, Y. Magnetic properties of ZnS doped with noble metals (X = Ru, Rh, Pd, and Ag). *J. Appl. Phys.* **2012**, *112*, 123920. [CrossRef]
67. Turek, I.; Kudrnovsky, J.; Diviš, M.; Franek, P.; Bihlmayer, G.; Blügel, S. First-principles study of the electronic structure and exchange interactions in bcc europium. *Phys. Rev. B* **2003**, *68*, 224431. [CrossRef]
68. Kim, Y.-S.; Chung, Y.-C.; Yi, S.-C. Electronic structure and half-metallic property of Mn-doped β-SiC diluted magnetic semiconductor. *Mater. Sci. Eng. B* **2006**, *126*, 194–196. [CrossRef]